Antoinette M. Maniatty[1]
Professor
Fellow ASME
Department of Mechanical,
Aerospace, and Nuclear Engineering,
Rensselaer Polytechnic Institute,
110 8th Street,
Troy, NY 12180
e-mail: maniaa@rpi.edu

Jiamin Ni
Department of Mechanical, Aerospace,
and Nuclear Engineering,
Rensselaer Polytechnic Institute,
110 8th Street,
Troy, NY 12180
e-mail: nij4@rpi.edu

Yong Liu
Distinguished Member of Technical Staff
Fairchild Semiconductor,
82 Running Hill Road,
South Portland, ME 04106
e-mail: yong.liu@fairchildsemi.com

Hongqing Zhang
Semiconductor Packaging Analysis,
IBM Microelectronics,
2070 Route 52,
Hopewell Junction, NY 12533
e-mail: zhangh@us.ibm.com

Effect of Microstructure on Electromigration-Induced Stress

In this paper, a finite element based simulation approach for predicting the effect of microstructure on the stresses resulting from electromigration-induced diffusion is described. The electromigration and stress-driven diffusion equation is solved coupled to the mechanical equilibrium and elastic constitutive equation, where a diffusional inelastic strain is introduced. Here, the focus is on the steady state, infinite life case, when the current-driven diffusion is balanced by the resulting stress gradient. The effect of the crystal orientation in Sn-based solder joints on the limiting current density for an infinite life is investigated and compared to experimental observations in the literature. The effect of the grain structure for Al interconnect lines on the dominant diffusion path and estimates for the effective charge number for two different diffusion paths in Al interconnects determined by matching simulations to experimental measurements of elastic strain components in the literature are also presented. [DOI: 10.1115/1.4031837]

1 Introduction

The microelectronics industry continues to attain increases in chip speeds while reducing cost and power consumption primarily through increasing device density and thus decreasing device dimensions. This downscaling of device dimensions leads to an increase in current density that must be carried by the metallic interconnects and solder bumps. With increased current density, electromigration-induced failure becomes a major reliability concern. Electromigration is a mass diffusion process attributed to momentum transfer from conducting electrons to diffusing metal atoms, which, over time, results in metal being depleted from the cathode end and accumulating at the anode end in a conductor [1–3]. If the conductor is confined, the depletion or accumulation of material leads to stress, with tensile stresses at the cathode and compressive stresses at the anode that drives a diffusion process in the reverse direction [4]. If the resulting stress gradient is sufficiently high, electromigration is arrested [5,6]. This leads to a prediction of a critical current density, below which electromigration is halted, that is inversely proportional to the line length.

The microstructure, in particular the grain structure, strongly impacts the stresses that develop and the time to failure resulting from electromigration in metal interconnects and solder bumps. The grain structure impacts the stress state primarily in two ways. First, the grain structure affects the diffusion path, which impacts where the diffusing material is depleted and accumulates ultimately affecting the stress state [7]. For example, in two electromigration experiments on aluminum (Al) interconnect lines, where the elastic strain resulting from the stress was measured in the direction perpendicular to the substrate, opposite trends were observed, which is attributable to the difference in the grain structures and dominant diffusion paths [8,9]. In Wang et al. [8], the Al line was relatively wide with multiple grains across the width of the line, and thus, the grain boundaries were the dominant diffusion path. On the other hand, in Zhang et al. [9], the Al line was narrow with closer to a bamboo structure with typically only one grain across the width, and thus, diffusion along the interfaces between the line and surrounding material dominated. Likewise, in tin (Sn)-based solder joints, the grain structure affects the dominant diffusion paths and the resulting stress state [10–13]. Second, because the diffusion and mechanical behavior of individual grains are anisotropic, the grain structure and orientations affect the stress state. For example, Sn-based solder is primarily composed of β Sn, which has a body-centered-tetragonal (bct) crystal lattice structure. When subjected to a current load, both self-diffusion and interstitial diffusion of the metallization layer occur with the rate of each diffusion mechanism being very different along the *a*- and *c*-axis [12,14–17].

Because electromigration has been identified as a serious reliability issue in integrated circuits, substantial effort has been devoted to modeling the phenomenon in order to design new integrated circuits that are not prone to electromigration-induced failure. Early work focused on analytical one-dimensional models for metallization lines [6,18]. In more recent years, computational and more sophisticated analytic models have been developed to more accurately model real interconnect geometries, the surrounding materials, and more complex physics. While most of these models treat the materials as homogeneous and do not account explicitly for microstructure nor the associated anisotropy, a few do consider microstructure explicitly.

[1]Corresponding author.

Contributed by the Applied Mechanics Division of ASME for publication in the Journal of Applied Mechanics. Manuscript received July 20, 2015; final manuscript received October 15, 2015; published online November 9, 2015. Assoc. Editor: Harold S. Park.

Several researchers have developed finite-element models that solve the mass diffusion equation including the current density, stress gradient, and temperature gradient as driving forces for diffusion, coupled with the electrical, mechanical, and thermal equations required to solve for the current density, stress, and temperature fields. Basaran and coworkers developed a 2D finite-element model that included plastic deformation in the stress analysis, which they compared to the experimental observations of the displacement field in a solder joint [19,20]. That research group more recently extended that model to 3D and added a damage metric to predict void growth and the resulting elastic modulus reduction [21]. The model was used to study the effect of temperature on the mean time to failure in solder at low temperatures. Singh et al. developed a 3D finite-element model for predicting the critical conditions to nucleate electromigration or stress-induced voids in interconnects, where they incorporate a cohesive zone model in the interfaces in order to model surface separation and mass diffusion in the surfaces [22]. Liu and coworkers have done extensive work in developing a 3D finite-element model for predicting void formation due to electromigration and reliability in wafer level packages [23–28]. While the above models have been able to provide some insight into where voids are likely to form and the effect of line geometry, current density, and temperature on void formation and failure, these models do not account for microstructure nor do they account for the strong anisotropy present in Sn-based solder.

A few researchers have developed numerical models that treat the metal interconnect as an aggregate of grains in order to capture the effect of the microstructure. A semi-analytic, 2D model for grain boundary diffusion in columnar grain structures was developed by Gleixner and Nix [29]. Povirk and Bower et al. proposed and implemented 2D finite-element formulations for polycrystalline interconnects that incorporated grain boundary, surface, and bulk diffusion explicitly [30–32]. Buchovecky et al. modeled 3D intermetallic compound (IMC) growth and stress-driven diffusion in a Sn film with a columnar grain structure [33]. In that model, the Sn grains are treated as isotropic, elastic–plastic, and the stress is induced in the Sn film from the transformation of Sn to IMC. A rigorous model that explicitly considers the stress and electromigration-driven diffusion along grain boundaries was developed by Wilkening et al. [34]. In that work, they show the conditions in which at steady state, the stress does not balance the electromigration driving force leading to progressive damage assuming isotropic elasticity and electrical behavior in the individual grains.

In this paper, we consider the effect of the microstructure on the resulting stress field due to electromigration, where we assume that the conductor is sufficiently short and confined to generate a large enough stress gradient so that electromigration is arrested. In this work, we consider the effects of the dominant diffusion path, the elastic anisotropy, and the electrical anisotropy. We consider cases involving both Sn-based solder connections and Al interconnects. By comparing simulations to experiments, we are able to elucidate new information about the effect of the crystal orientations on the limiting current density for a given line length in Sn-based solder joints and the effect of grain structure on the dominant diffusion path in Al interconnects. We are also able to estimate the effective charge number for Al interconnect for two different diffusion paths.

2 Governing Equations and Problem Definition

Let $\mathcal{B}$ be the region of interest that includes both the conducting and surrounding materials, and let $\mathcal{B}_c \subset \mathcal{B}$ be the region with the conducting material where electromigration occurs. The atomic flux vector, $\boldsymbol{J}$, resulting from the current $\boldsymbol{j}$ and driving stress $\bar{\sigma}$ in $\mathcal{B}_c$ is given by [18]

$$\boldsymbol{J} = \frac{\boldsymbol{D}}{\Omega k T}(-e\boldsymbol{Z}^{\star}\boldsymbol{\rho}\boldsymbol{j} + \Omega\nabla\bar{\sigma}) \tag{1}$$

where $\boldsymbol{D}$ is the diffusivity, Ω is the atomic volume, k is the Boltzmann constant, T is the temperature, e is the elementary charge, $\boldsymbol{Z}^{\star}$ is the effective charge number tensor, and $\boldsymbol{\rho}$ is the electrical resistivity tensor. The first term in Eq. (1) is the driving force due to the current, and the second term is the mechanical driving force. The appropriate scalar driving stress $\bar{\sigma}$ is determined by the dominant diffusion path, which, in turn, depends on the microstructure. For grain boundary diffusion, the driving stress is taken as the normal stress on the grain boundaries [6,18,29,30], while for lattice diffusion, the driving stress is the hydrostatic stress [7,8,35]. Other dominant diffusion paths, such as interface diffusion, would be associated with other definitions of the driving stress, which is discussed further below.

While for crystals with cubic symmetry, such as Al, the effective charge number and electrical resistivity are isotropic and these parameters reduce to scalars, for materials such as Sn-based solder, which has a bct crystal structure, the effective charge number and electrical resistivity are different along the a and c crystal directions, and thus, must be treated as tensors.

The rate of accumulation or depletion of a volume of atoms per unit volume at a given location in $\mathcal{B}_c$ may then be expressed as

$$\frac{\partial\gamma}{\partial t} = -\Omega\nabla\cdot\boldsymbol{J} \tag{2}$$

where γ represents a local inelastic dilatation. If the only source of inelastic deformation is the local change in the volume of atoms due to diffusion; then, the local inelastic strain tensor $\boldsymbol{\varepsilon}^i$ should be such that

$$\mathrm{tr}(\boldsymbol{\varepsilon}^i) = \gamma \tag{3}$$

If we further assume coordinates that align with the principal directions of inelastic straining, then

$$\boldsymbol{\varepsilon}^i = \gamma\boldsymbol{H} = \gamma\begin{bmatrix} a_1 & 0 & 0 \\ 0 & a_2 & 0 \\ 0 & 0 & a_3 \end{bmatrix} \tag{4}$$

where $a_1 + a_2 + a_3 = 1$. The relative values of a_1, a_2, and a_3 depend on where the diffusing atoms are removed and deposited, i.e., how the material arranges itself on the downstream end and is depleted on the upstream end, which depends on the diffusion paths. For example, if interface diffusion dominates and the normal to the interface is aligned with the x_3 coordinate direction, then it may be reasonable to assume $a_1 = a_2 = 0$ and $a_3 = 1$, as the atoms will be removed and deposited in the interface causing the material to grow or shrink in this direction. It should also be noted that the tensor $\boldsymbol{H}$ relates the scalar driving stress $\bar{\sigma}$ to the stress tensor $\boldsymbol{\sigma}$ such that

$$\bar{\sigma} = \boldsymbol{H}:\boldsymbol{\sigma} = \mathrm{tr}(\boldsymbol{H}^{\mathrm{T}}\boldsymbol{\sigma}) \tag{5}$$

where : indicates a double contraction. This form of $\boldsymbol{H}$ assumes an average effect of the diffusion over the volume and is a reasonable assumption for single crystals, for interface-dominated diffusion with parallel flat interfaces, and for grain boundary diffusion when there are many grains across the region of interest. However, this assumption would not be valid for modeling grain boundary diffusion when there are only a few grains in a region and other cases where the diffusing material would take paths that vary. In those cases, the details of the microstructure would need to be considered explicitly in defining the form of the inelastic strain and driving stress, which would vary throughout the volume of the conducting material.

If the conducting material is constrained, then stresses will result from the inelastic strain. Assuming small deformations and linear elasticity, the stress is then

$$\boldsymbol{\sigma} = \mathcal{L}:(\boldsymbol{\varepsilon}^e), \quad \boldsymbol{\varepsilon}^e = \boldsymbol{\varepsilon} - \boldsymbol{\varepsilon}^i \tag{6}$$

where $\mathcal{L}$ is the fourth-order elasticity tensor, $\boldsymbol{\varepsilon}^e$ is the elastic strain, and the strain $\boldsymbol{\varepsilon}$ may be expressed in terms of the displacement field $\boldsymbol{u}$ as

$$\boldsymbol{\varepsilon} = \frac{1}{2}(\nabla \boldsymbol{u} + \nabla \boldsymbol{u}^{\mathrm{T}}) \tag{7}$$

If thermal strains are present, the above equation could be expanded to include those as well, which would depend on the temperature history. The resulting stress state in the conducting and surrounding materials, region $\mathcal{B}$, must be in equilibrium, and thus, the stress state should satisfy

$$\nabla \cdot \boldsymbol{\sigma} = \mathbf{0} \tag{8}$$

In this work, we focus on the case where electromigration is arrested due to stresses resulting from confinement. When this occurs, $\boldsymbol{J} = \mathbf{0}$, and Eq. (1) yields

$$\nabla \bar{\sigma} = \frac{e}{\Omega} \boldsymbol{Z}^{\star} \boldsymbol{\rho} \boldsymbol{j} \tag{9}$$

Combining Eqs. (4)–(9) and assuming the usual symmetries in $\mathcal{L}$, the problem can then be defined as: find the volumetric inelastic dilatation γ resulting from electromigration and induced displacement field $\boldsymbol{u}$ that satisfy

$$\nabla \cdot [\mathcal{L} : (\nabla \boldsymbol{u} - \gamma \boldsymbol{H})] = \mathbf{0} \quad \text{in } \mathcal{B} \tag{10}$$

$$\nabla [\boldsymbol{H} : \mathcal{L} : (\nabla \boldsymbol{u} - \gamma \boldsymbol{H})] = \frac{e}{\Omega} \boldsymbol{Z}^{\star} \boldsymbol{\rho} \boldsymbol{j} \quad \text{in } \mathcal{B}_c \tag{11}$$

for a given current density field $\boldsymbol{j}$ subject to boundary conditions

$$\boldsymbol{u} = \check{\boldsymbol{u}} \quad \text{on } \mathcal{S}_u \tag{12}$$

$$\boldsymbol{\sigma} \boldsymbol{n} = \check{\boldsymbol{T}} \quad \text{on } \mathcal{S}_T \tag{13}$$

where $\check{\boldsymbol{u}}$ represents a prescribed displacement on boundary $\mathcal{S}_u$, $\boldsymbol{n}$ is the outward unit normal on the boundary, and $\check{\boldsymbol{T}}$ represents a prescribed traction on boundary $\mathcal{S}_T$. The boundary conditions are specified on the entire boundary $\mathcal{S}$ of region $\mathcal{B}$ without overlap such that $\mathcal{S}_u \cup \mathcal{S}_T = \mathcal{S}$ and $\mathcal{S}_u \cap \mathcal{S}_T = \varnothing$. In addition, since diffusion only occurs in the conducting material, γ is only nonzero in $\mathcal{B}_c$. Furthermore, we expect that the material accumulated and depleted throughout the conducting material must balance to satisfy mass balance, and thus

$$\int_{\mathcal{B}_c} \gamma dV = 0 \tag{14}$$

If all the parameters other than the solution variables $\boldsymbol{u}$ and γ are known, Eqs. (10) and (11) represent a set of six equations with four unknowns, with Eq. (14) as an additional constraint on the solution of γ. However, $\boldsymbol{H}$, which is associated with the diffusion path, and the effective charge number(s) defining $\boldsymbol{Z}^{\star}$ are typically not well-known and may also be treated as unknowns that need to be solved for. In that case, additional information, such as measurements of elastic strain components, are required to solve for these parameters as well as $\boldsymbol{u}$ and γ. Here, we will consider both cases where $\boldsymbol{H}$ and $\boldsymbol{Z}^{\star}$ are assumed known as well as cases where they are not completely known, but elastic strain measurements are available [8,9].

3 Finite-Element Model and Solution Approach

A finite-element formulation is used to define a discrete set of equations. The displacement field $\boldsymbol{u}$ and inelastic dilatation γ are approximated in terms of finite-element basis functions such that

$$\boldsymbol{u}(\boldsymbol{x}) \approx \tilde{\boldsymbol{u}}(\boldsymbol{x}) = \tilde{\boldsymbol{u}}_{\alpha} \psi_{\alpha}(\boldsymbol{x}) \quad \alpha = 1, N \tag{15}$$

$$\gamma(\boldsymbol{x}) \approx \tilde{\gamma}(\boldsymbol{x}) = \tilde{\gamma}_{\beta} \psi_{\beta}(\boldsymbol{x}) \quad \beta = 1, N_c \tag{16}$$

where $\tilde{\boldsymbol{u}}$ and $\tilde{\gamma}$ are finite dimensional approximations of $\boldsymbol{u}$ and γ, ψ_{α} are finite-element basis functions, N is the number of nodes for the displacement interpolation in $\mathcal{B}$, and N_c is the number of nodes for the inelastic dilatation interpolation in $\mathcal{B}_c$. Summation is implied on the repeated Greek subscripts. Equation (10) together with boundary conditions (12) and (13) is analogous to a thermal–elastic problem. Substituting the interpolations into a standard Galerkin formulation yields the following:

$$\int_{\mathcal{B}} [\mathcal{L} : (\nabla \tilde{\boldsymbol{u}} - \tilde{\gamma} \boldsymbol{H})] : \nabla \tilde{\boldsymbol{v}} dV - \int_{\mathcal{S}_T} \check{\boldsymbol{T}} \cdot \tilde{\boldsymbol{v}} dA = 0 \tag{17}$$

where $\tilde{\boldsymbol{v}}$ is a finite dimensional variation, which is interpolated with the same interpolations as $\tilde{\boldsymbol{u}}$. Forming a variational form of Eq. (11) and substituting in the interpolations result in

$$\int_{\mathcal{B}_c} \left\{ \nabla [\boldsymbol{H} : \mathcal{L} : (\nabla \tilde{\boldsymbol{u}} - \tilde{\gamma} \boldsymbol{H})] - \frac{e}{\Omega} \boldsymbol{Z}^{\star} \boldsymbol{\rho} \boldsymbol{j} \right\} \cdot \tilde{\boldsymbol{v}} dV = 0 \tag{18}$$

or the weak form

$$\int_{\mathcal{B}_c} \left[\boldsymbol{H} : \mathcal{L} : (\nabla \tilde{\boldsymbol{u}} - \tilde{\gamma} \boldsymbol{H})(\nabla \cdot \tilde{\boldsymbol{v}}) + \left(\frac{e}{\Omega} \boldsymbol{Z}^{\star} \boldsymbol{\rho} \boldsymbol{j} \right) \cdot \tilde{\boldsymbol{v}} \right] dV - \int_{\mathcal{S}_c} [\boldsymbol{H} : \mathcal{L} : (\nabla \tilde{\boldsymbol{u}} - \tilde{\gamma} \boldsymbol{H})] \boldsymbol{n} \cdot \tilde{\boldsymbol{v}} dA = 0 \tag{19}$$

where $\mathcal{S}_c$ is the boundary of $\mathcal{B}_c$. While Eq. (17) is standard, Eqs. (18) and (19) each have their own challenges, Eq. (18) because of the gradient term, and Eq. (19) because of the boundary term. In this work, we use Eq. (18). In addition, we have the challenges that $\boldsymbol{H}$ and $\boldsymbol{Z}^{\star}$ may not be fully defined, or if they are prescribed, they may not be accurate. Moreover, we have not yet brought into the formulation the constraint Eq. (14) or how to consider measured elastic strains if available. We shall consider some of these cases next as we develop solution approaches.

The overall approach we take here is a staggered approach, where we alternately solve Eq. (18) for a best fit of $\tilde{\gamma}$ and any additional unknown parameters while keeping $\tilde{\boldsymbol{u}}$ fixed, and then solve Eq. (17) for $\tilde{\boldsymbol{u}}$ while keeping $\tilde{\gamma}$ and $\boldsymbol{H}$ fixed until convergence. This can be thought of as first perfectly confining the material so there is no displacement, and solving for the inelastic strain resulting from current-driven diffusion, then allowing the material to relax and self-equilibrate, and repeating this sequence until the computed inelastic strain field no longer changes and is in equilibrium with the displacement field.

3.1 Case 1: Fully Prescribed Diffusion Parameters and No Elastic Strain Measurements.

For this case, the dominant diffusion path is assumed known as well as the effective charge number(s), and thus $\boldsymbol{H}$ and $\boldsymbol{Z}^{\star}$ are fully prescribed, and no additional information regarding the elastic strains is given. This could be thought of as the typical forward modeling case. Here, we use Eq. (18) together with the constraint (14) and we assume the conducting material is locally homogeneous. Symbolically, after substituting in finite-element interpolations into Eq. (18), a linear system of the following form results:

$$\mathbf{L}\mathbf{d} = \mathbf{b} \tag{20}$$

where $\mathbf{d}$ represents the vector of nodal inelastic dilatations $\tilde{\gamma}_{\beta}$, $\beta = 1, N_c$, and for clarity, $\mathbf{L}$ and $\mathbf{b}$ are defined indicially

$$L_{i\alpha\beta} = \int_{\mathcal{B}_c} H_{jk} \mathcal{L}_{jklm} H_{lm} \frac{\partial \psi_{\beta}}{\partial x_i} \psi_{\alpha} dV \tag{21a}$$

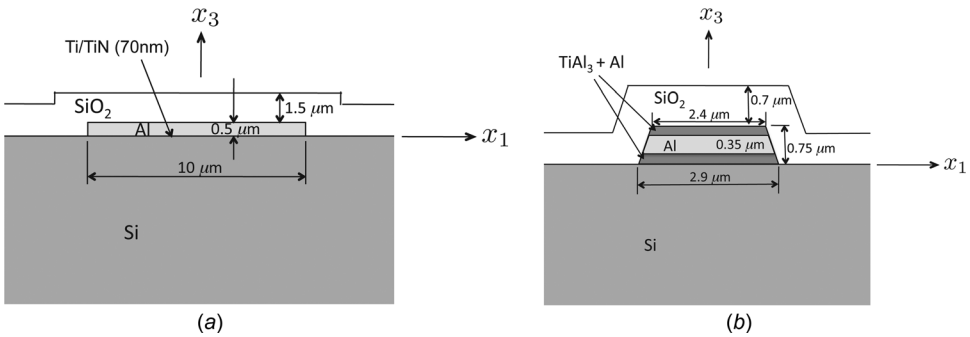

Fig. 1 Cross-sectional diagrams of Al interconnect lines from the experiments by (*a*) Wang et al. [8] and (*b*) Zhang et al. [9]

$$b_{i\alpha} = \int_{\mathcal{B}_c} \left[\frac{\partial}{\partial x_i} \left(H_{jk} \mathcal{L}_{jklm} \frac{\partial \tilde{u}_l}{\partial x_m} \right) - \frac{e}{\Omega} Z^{\star}_{ij} \rho_{jk} j_k \right] \psi_{\alpha} dV \tag{21b}$$

where Latin subscripts indicate dimension, and summation is implied on repeated indices. The first term in the integrand in Eq. (21*b*) is found by locally reconstructing $\nabla \tilde{\boldsymbol{u}}$ at the nodes, following the method presented in Maniatty et al. [36], and then differentiating the term in parentheses as usual with the shape function derivatives. In three-dimensional (3D), the above system represents $3N_c$ equations with N_c unknowns. We seek to find $\mathbf{d}$ that best satisfies Eq. (20) and constraint (14). To do this, we minimize the following function:

$$m_1 = \frac{1}{2} \left[(\mathbf{L}\mathbf{d} - \mathbf{b})^{\mathrm{T}} (\mathbf{L}\mathbf{d} - \mathbf{b}) + \lambda_1 (\mathbf{d} \cdot \mathbf{w})^2 \right] \tag{22}$$

where

$$\mathbf{d} \cdot \mathbf{w} = \tilde{\gamma}_{\beta} w_{\beta} = \tilde{\gamma}_{\beta} \int_{\mathcal{B}_c} \psi_{\beta} dV \tag{23}$$

and λ_1 is a constant coefficient that defines how strongly the constraint is applied. Minimizing m_1 with respect to $\mathbf{d}$ yields the following system:

$$(\mathbf{L}^{\mathrm{T}}\mathbf{L} + \lambda_1 \mathbf{w}\mathbf{w}^{\mathrm{T}})\mathbf{d} = \mathbf{L}^{\mathrm{T}}\mathbf{b} \tag{24}$$

that is used to update $\mathbf{d}$ ($\tilde{\gamma}$). We then solve Eq. (17) for $\tilde{\boldsymbol{u}}$, given $\tilde{\gamma}$, using a standard finite-element method. We continue to alternately solve these two systems until convergence is achieved on $\mathbf{d}$ and $\tilde{\boldsymbol{u}}$ when $||\mathbf{d}^{(r+1)} - \mathbf{d}^{(r)}||/||\mathbf{d}^{(r+1)}|| < \text{toler}$ and $||\tilde{\boldsymbol{u}}^{(r+1)} - \tilde{\boldsymbol{u}}^{(r)}||/||\tilde{\boldsymbol{u}}^{(r+1)}|| < \text{toler}$ ($||\cdot||$ indicates L_2 norm), where r indicates iterations and toler is a prescribed tolerance.

3.2 Case 2: Unknown Diffusion Parameters and Some Elastic Strain Measurements. In this case, we use measurements of elastic strain together with the governing equations in Sec. 2 to determine both the inelastic dilatation γ distribution, the effective charge number $Z^{\star}$ and, where possible, the parameters defining $\boldsymbol{H}$, which are associated with the dominant diffusion path. This case is motivated by the experiments conducted in Cargill's group on Al interconnect lines, described in Refs. [8] and [9], where components of the elastic strain were measured using X-ray microbeam diffraction while the lines were subjected to high-current densities. Schematics showing the cross section of each line from those experiments are shown in Fig. 1. In both experiments, the elastic strain perpendicular to the substrate (ε^e_{33}) was measured along the length of the line and is shown in Fig. 2. As can be seen, the data from these two experiments show opposite trends. In Wang et al. [8], the Al line was relatively wide, and there were multiple grains across the width of the line, while in Zhang et al. [9], the line was narrower with typically only one grain across the width. In addition, in Zhang et al. [9], the Ti liner layers reacted with the Al forming very fine grain Ti rich layers above and below the Al line. The different trends in the measured elastic normal strains may be attributed to the difference in the microstructures of these two lines. In Zhang et al., all of the components of the deviatoric elastic strains were also measured using Laue white-beam diffraction. Finally, it should be noted that in Zhang et al., it was postulated that the passivation layer may have delaminated at the downstream end leading to the stresses, and thus the strains, leveling off rather than continuing to grow in magnitude.

As in case 1, we use the finite-element formulation defined by Eqs. (17) and (18), however, in this case, $Z^{\star}$ is treated as an unknown. For the moment, we assume $\boldsymbol{H}$ is known. For Al, since $Z^{\star}$ and ρ are scalars, and we know $\boldsymbol{j}$, we can multiply Eq. (18) by a tensor that extracts components orthogonal to $\boldsymbol{j}$ and thus eliminates that term. In this case, since the current is along the length of the line (along x_2), this effectively converts this to a 2D equation in the x_1–x_3 plane, i.e., Eq. (18) is solved in the cross-sectional planes, rather than over the volume $\mathcal{B}_c$ at different locations along the length of the line with the constraint that the resulting average elastic strain ε^e_{33} matches the measured value at that location. Thus, at a given cross section, we have the linear system (20), where now $\mathbf{b}$ is replaced with $\mathbf{b}^2$ defined as

$$b^2_{i\alpha} = \int_{\mathcal{A}_c} \frac{\partial}{\partial x_i} \left(H_{jk} \mathcal{L}_{jklm} \frac{\partial \tilde{u}_l}{\partial x_m} \right) \psi_{\alpha} dA \tag{25}$$

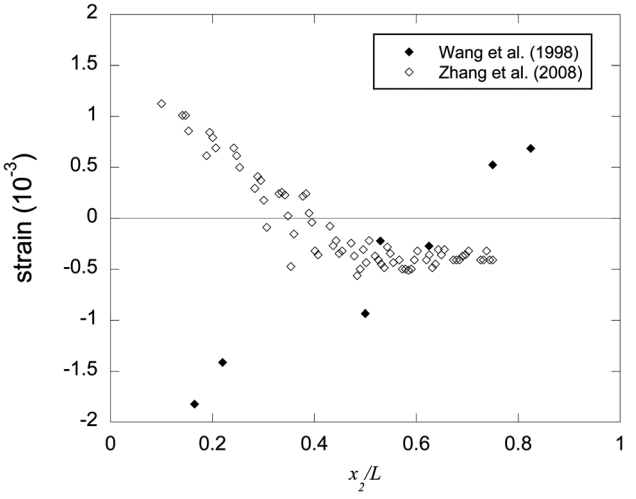

Fig. 2 Comparison of the measured normal elastic strain ε^e_{33} as a function of distance from the cathode end, normalized by the line length *L*, for Al conductor lines in Wang et al. [8] and Zhang et al. [9]

where now $i=1$ and 3, and the integrals defining both $\mathbf{L}$ and $\mathbf{b}^2$ are over the cross section of the Al conductor line $\mathcal{A}_c$. In order to satisfy the governing equation and best match the measured elastic strain, we define the minimization problem

$$m_2 = \frac{1}{2}\left[(\mathbf{Ld}-\mathbf{b}^2)^{\mathrm{T}}(\mathbf{Ld}-\mathbf{b}^2)+\lambda_2\left(\mathbf{d}\cdot\mathbf{q}-\mathcal{A}_c\langle\tilde{\varepsilon}_{33}\rangle+\mathcal{A}_c\varepsilon_{33}^{e(m)}\right)^2\right] \tag{26}$$

where

$$\mathbf{d}\cdot\mathbf{q}=\tilde{\gamma}_\beta q_\beta=\tilde{\gamma}_\beta\int_{\mathcal{A}_c}H_{33}\psi_\beta dA,\quad \langle\tilde{\varepsilon}_{33}\rangle=\frac{1}{\mathcal{A}_c}\int_{\mathcal{A}_c}\tilde{u}_{3\alpha}\frac{\partial\psi_\alpha}{\partial x_3}dA \tag{27}$$

$<\cdot>$ indicates the area average, and superscript (m) indicates the measured value. Minimizing m_2 with respect to $\mathbf{d}$ yields the following system:

$$(\mathbf{L}^{\mathrm{T}}\mathbf{L}+\lambda_2\mathbf{q}\mathbf{q}^{\mathrm{T}})\mathbf{d}=\mathbf{L}^{\mathrm{T}}\mathbf{b}^2+\lambda_2\mathcal{A}_c(\langle\tilde{\varepsilon}_{33}\rangle-\varepsilon_{33}^{e(m)})\mathbf{q} \tag{28}$$

that is used to update $\mathbf{d}$ $(\tilde{\gamma})$ in each cross section.

It still remains to define the components of $\boldsymbol{H}$. For the given geometry, since the current is along x_2 and due to the geometric symmetry, it is reasonable to assume that the principal diffusion directions are aligned with the coordinates shown in Fig. 1, and thus, $\boldsymbol{H}$ has the form in Eq. (4) so that only a_1, a_2, and a_3 (a_i) need to be defined with the constraint $a_1+a_2+a_3=1$. For the Wang et al. [8] case, we do not have any additional information, so we assume values for a_i, and then see if the solution is reasonable, which will be described in more detail in Sec. 4.2. For the Zhang et al. [9] case, we also have measurements of the deviatoric elastic strain, which may be used to update $\boldsymbol{H}$. The deviatoric elastic strain, $\boldsymbol{\varepsilon}^{e\prime}$, is related to $\boldsymbol{H}$ as

$$\boldsymbol{\varepsilon}^{e\prime}=\boldsymbol{\varepsilon}^{e}-\frac{1}{3}\mathrm{tr}(\boldsymbol{\varepsilon}^{e})\boldsymbol{I}=\boldsymbol{\varepsilon}-\gamma\boldsymbol{H}-\frac{1}{3}[\mathrm{tr}(\boldsymbol{\varepsilon})-\gamma]\boldsymbol{I} \tag{29}$$

where $\boldsymbol{I}$ is the identity tensor. We only have measurements of the average deviatoric elastic strain at different locations along the length of the line, and assuming $\boldsymbol{H}$ is diagonal with a trace equal to one, then we can solve for the diagonal components of $\boldsymbol{H}$ in each cross section

$$a_i^c=\frac{1}{\langle\tilde{\gamma}\rangle}\left[\langle\varepsilon_{ii}\rangle-\varepsilon_{ii}^{e\prime(m)}-\frac{1}{3}\left(\langle\mathrm{tr}(\boldsymbol{\varepsilon})\rangle-\langle\tilde{\gamma}\rangle\right)\right]\quad(\text{no sum on } i) \tag{30}$$

where the superscript c indicates for a cross section $\mathcal{A}_c$. Finally, we assume that the diffusion path is the same everywhere in an average sense and set a_i to be the average values over all the cross sections.

A summary of the algorithm is as follows:

(1) Select values for $a_1^{(p)}$, $a_2^{(p)}$, and $a_3^{(p)}$ and initialize $\gamma^{(r)}=\gamma_0(x_3)$ (uniform in cross sections), where superscripts $p=0$ and $r=0$ indicate outer and inner iterations. The initial value of $\gamma_0(x_3)$ is found by matching the measured $\varepsilon_{33}^{e(m)}$ along the line length by increasing or decreasing $\gamma_0(x_3)$ at each cross section.
(2) Solve Eq. (28) for $\mathbf{d}^{(r+1)}$ (nodal values of $(\tilde{\gamma})^{(r+1)}$) on the Al line cross sections $\mathcal{A}_c$ along the length of the line.
(3) Solve Eq. (17) for $\tilde{\boldsymbol{u}}^{(r+1)}$ on the volume of the line and surrounding material $\mathcal{B}$.
(4) If $||\mathbf{d}^{(r+1)}-\mathbf{d}^{(r)}||/||\mathbf{d}^{(r+1)}||<$ toler and $||\tilde{\boldsymbol{u}}^{(r+1)}-\tilde{\boldsymbol{u}}^{(r)}||/||\tilde{\boldsymbol{u}}^{(r+1)}||<$ toler, then converged on $\mathbf{d}$ and $\tilde{\boldsymbol{u}}$ and go to step 6, else continue.
(5) $\mathbf{d}^{(r+1)}\rightarrow\mathbf{d}^{(r)}$, $\tilde{\boldsymbol{u}}^{(r+1)}\rightarrow\tilde{\boldsymbol{u}}^{(r)}$, go to step 2.
(6) If measurements of the deviatoric elastic strains are not available, done, else continue.
(7) Solve for $a_1^{(p+1)}$, $a_2^{(p+1)}$, and $a_3^{(p+1)}$ using Eq. (30) on each cross section $\mathcal{A}_c$ and averaging over the cross sections.
(8) If $||\boldsymbol{a}^{(p+1)}-\boldsymbol{a}^{(p)}||/||\boldsymbol{a}^{(p+1)}||<$ toler, then go to step 10, else continue.
(9) (9) $\boldsymbol{a}^{(p+1)}\rightarrow\boldsymbol{a}^{(p)}$, go to step 2.
(10) Compute Z^* from Eq. (9) using $\bar{\sigma}$ computed from the simulation and prescribed current density $\boldsymbol{j}$.

4 Results and Discussion

We apply the methods described above to Sn-based solder joints and Al interconnects. For the Sn-based solder joint, we do not have measurements of elastic strain available and we use the approach outlined in Sec. 3.1, while for the Al interconnects, we follow the approach described in Sec. 3.2. For both cases, we compare to data from the literature to draw conclusions about microstructure effects.

4.1 Solder Joints. Since Sn makes up more than 95% of the lead-free solder joints and the joints are usually comprised of one or a few β-Sn grains, the orientation of these grains has a big effect on the electromigration-induced degradation. In Lu et al. [17], two damage modes were identified, where the damage mode depended strongly on the local grain orientation. Mode I damage is associated with Sn self-diffusion and is dominant when the crystal c-axis is perpendicular, or strongly misaligned, relative to the current direction. Mode II damage is associated with fast interstitial diffusion of nickel (Ni) and copper (Cu) along the crystal c-axis and is thus dominant when the c-axis is aligned with the current direction and the Sn connects to Ni or Cu. Furthermore, mode II damage is suppressed in SnAg solder, while mode II is more common in SnCu solder. In this work, we consider only the case of self-diffusion, i.e., mode I as described in Lu et al. [17], investigating the effect of the crystal orientation, assuming a single crystal solder joint.

We model a simplified flip-chip-like Sn-based solder joint described in Lu et al. [37], which was designed so that the current density is uniform along the axis of the solder joint. In that work, the threshold product of the current density magnitude times the line length (L) at which electromigration is arrested, the so-called Blech limit, was measured for Sn1.8Ag solder joints and was found to be $jL=30$ A/cm. However, there is considerable scatter in the data presented in that paper, and the Blech limit appears to be anywhere in the range $3\leq jL\leq 55$ A/cm depending on the sample. We believe that this may be largely attributed to the effect of the grain orientation, which is studied here.

The solder connection is cylindrical with a diameter of 287 μm and the thickness is chosen to be 57.69 μm, which is within the range of thicknesses studied in Lu et al. [37] and which is at the

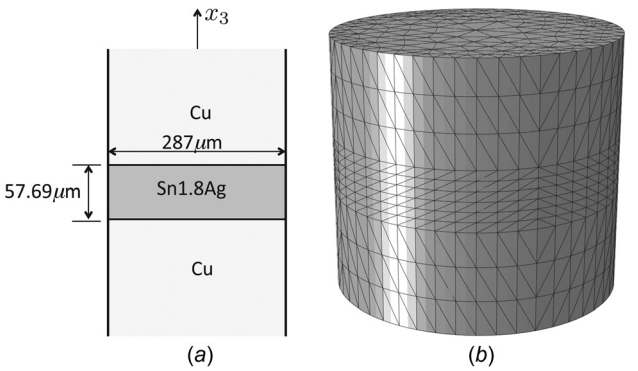

Fig. 3 (*a*) Cu–solder–Cu structure as in Ref. [37] and (*b*) model mesh

average Blech limit of 30 Am/cm when a current density of 5200 A/cm^2 is applied. The solder is attached to Cu wires at the two ends as shown in Fig. 3(*a*). There were also thin IMC and nickel layers between the Cu and Sn1.8Ag in the experiment that are not included in our model. The microstructures of the solder connections were not reported in Lu et al. [37]. Here, we assume the connection is a single crystal, and thus, diffusion is through the lattice. For lattice diffusion, it is reasonable to assume $a_1 = a_2 = a_3 = (1/3)$ in Eq. (4), and then, the scalar driving stress is the hydrostatic stress $\bar{\sigma} = (1/3)(\sigma_{11} + \sigma_{22} + \sigma_{33})$ from Eq. (5). It should be noted that even for an arbitrarily elastic anisotropic material, the stress state about a vacancy is hydrostatic, and thus, the gradient in the hydrostatic stress is expected to be the driving force for atom-vacancy exchanges, the mechanism for lattice diffusion. The effective charge numbers along the *a* and *c* crystal directions are taken as $Z_a^\star = 16$ and $Z_c^\star = 10$ [38]. The nonzero components in the electrical resistivity tensor $\boldsymbol{\rho}$ are $\rho_a = 14.84\ \mu\Omega$ cm and $\rho_c = 10.47\ \mu\Omega$ cm at 141 °C (the experimental temperature in Ref. [37]) calculated from the data given in Ref. [39]. The elastic constants of single crystal Sn-based solder used, with respect to the lattice configuration, are $\hat{C}_{11} = 72.3$ GPa, $\hat{C}_{33} = 88.4$ GPa, $\hat{C}_{12} = 59.4$ GPa, $\hat{C}_{13} = 35.8$ GPa, $\hat{C}_{44} = 22.0$ GPa, and $\hat{C}_{66} = 24.0$ GPa [40]. The copper is treated as isotropic with elastic modulus $E_{\mathrm{Cu}} = 124$ GPa and Poisson's ratio $\nu_{\mathrm{Cu}} = 0.34$. The atomic volume for Sn is $\Omega = 2.71 \times 10^{-23}$ cm^3, and for completeness, the elementary charge is $e = 1.602 \times 10^{-19}$ C.

We use the procedure outlined in Sec. 3.1 to solve for the electromigration-induced dilatational strain γ and the displacement field $\boldsymbol{u}$ for a prescribed current density $\boldsymbol{j}$. The model and finite-element mesh we used are shown in Fig. 3(*b*). The top and bottom face of Cu is fixed in the x_3-direction. Rotation about the x_3-axis is also fixed. The finite-element mesh had 11,244 ten-node tetrahedral elements. Simulations are first done with the *c*-axis of the tin crystal aligned vertically (along x_3), and then with the gradual rotation of the crystal about the *a*-axis until the *c*-axis is horizontal. We use Bunge Euler angles [0 Φ 0] to represent the crystal orientation, where Φ is the angle that the *c*-axis deviates from x_3. When the *c*-axis is aligned either vertically (Φ = 0) or horizontally (Φ = 90 deg), the electromigration driving force $(-e\boldsymbol{Z}^\star\boldsymbol{\rho}\boldsymbol{j})$ is in the opposite direction as the current density ($\boldsymbol{j}$) which is in the $+x_3$ direction, and thus the gradient of the hydrostatic stress is also vertical and constant as defined in Eq. (9). When Φ = 0, $\partial\bar{\sigma}/\partial x_3 = 0.32\ \mathrm{MPa}/\mu\mathrm{m}$ and when Φ = 90 deg, $\partial\bar{\sigma}/\partial x_3 = 0.73\ \mathrm{MPa}/\mu\mathrm{m}$, for a current density of 5200 A/cm^2. For these two cases, the hydrostatic stress goes from compressive on the bottom, where material is accumulating, to tensile on the top, where material is being depleted. When the *c*-axis of the crystal is neither vertical nor horizontal, the electromigration driving force $(-e\boldsymbol{Z}^\star\boldsymbol{\rho}\boldsymbol{j})$ is not along the same axis as the current density ($\boldsymbol{j}$), and the hydrostatic stress has a more complicated distribution.

We determine the Blech limit by finding the current at which the crystal starts to yield, which is when the resolved shear stress τ^α on any of the slip system exceeds the critical resolved shear stress for that slip system, where

$$\tau^\alpha = \boldsymbol{s}^\alpha \cdot \boldsymbol{\sigma} \cdot \boldsymbol{m}^\alpha \tag{31}$$

and where $\boldsymbol{s}^\alpha$ and $\boldsymbol{m}^\alpha$ are the slip direction and slip plane normal, respectively. Zhou et al. [41] categorized commonly observed slip systems for bct β-Sn into ten-slip system families and slip in [001] and [111] directions is proved to be most facile. Here, we look at the resolved shear stress on the most active four slip systems ((010)[001], (1–10)[001], (010)[100], and (110)[1–11]/2). The critical resolved shear stresses for these four slip systems have been estimated to be 1.9 MPa, 1.3 MPa, 3.3 MPa, and 2.3 MPa [42]. We do not expect the Blech limit to occur as soon as a single location in the crystal yields, but when some larger-scale yielding occurs. Here, we define it as when 10% of the crystal yields. The predicted Blech limit, using this assumption, for crystals with different orientations is shown in Fig. 4. We see that when the crystal is oriented with its *c*-axis along the current direction, the Blech limit is highest with a value of $jL = 14.11$ A/cm, while the Blech limit is lowest when the *c*-axis is perpendicular to the current direction with a value of $jL = 4.05$ A/cm. The predicted values are within the range expected, but lower, on average, than expected. This may be because we assume that the Blech limit occurs when yielding occurs on any of the slip systems at 10% of the solder joint volume, but failure may not occur until a larger region yields. A more accurate estimate could be made by considering crystal plasticity, which will be the focus of future work.

4.2 Aluminum Interconnect Lines. Here, we model the Al interconnect lines studied experimentally in Refs. [8] and [9], described in Sec. 3.2 and shown in Fig. 1, where components of the elastic strain were measured using X-ray microbeam diffraction while the lines were subjected to high-current densities, and we back out values for $Z^\star$ and the components of the tensor $\boldsymbol{H}$. In Wang et al. [8], the elastic strain component ε_{33}^e was measured along the lengths of Al conductor lines that were 200 μm long, 10 μm wide, and 0.5 μm thick, with a 1.5 μm SiO_2 passivation layer and a Si (100) substrate, as shown in Fig. 1(*a*). There was also a 10 nm Ti/60 nm TiN shunt layer under the line, which is not shown in the schematic. The grain structure in the Al lines was columnar with average grain size roughly the same as the film thickness and had a strong ⟨111⟩ fiber texture, with the ⟨111⟩ crystal direction preferentially oriented along the x_3-direction. The experimental temperature was 260 °C, and the current density was 1.4×10^5 A/cm^2. In that experiment, the strain ε_{33}^e was found to increase (become more tensile) linearly along the direction of electron flow as shown in Fig. 2. In Zhang et al. [9], both the elastic strain component ε_{33}^e and all the components of the elastic, deviatoric strain tensor $\boldsymbol{\varepsilon}^{e\prime}$ were measured, in separate experiments, throughout two Al conductor lines with nominally the same structure. The lines were approximately 30 μm long, 2.6 μm wide, and 0.75 μm thick, with a 0.7 μm SiO_2 passivation layer and a Si (100) substrate. The grain structure consisted of polycrystalline (< 100 nm grain size), Ti rich layers (probably mixture of Al and $TiAl_3$) above and below the central part of the line, each about 0.2 μm thick, and micron-size columnar Al grains of about 0.35 μm thickness in the central part of the line, as depicted in Fig. 1(*b*). The Al grains had a strong ⟨111⟩ fiber texture. The experimental temperature was 190 °C and the applied current was 30 mA corresponding to a current density of 2.1×10^6 A/cm^2 if we assume the $TiAl_3$ takes up approximately 30% of the cross section area and the current only travels through the Al part of the line as the resistivity of $TiAl_3$ is much higher than that of Al. In

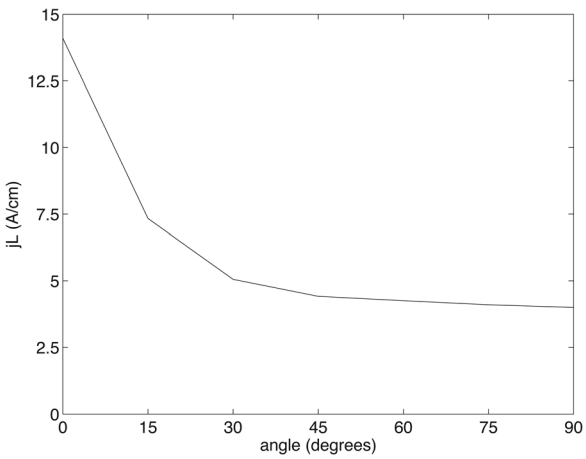

Fig. 4 The predicted Blech limit, threshold value of *jL* for which the solder is predicted to have an infinite life, as a function of the angle that the crystal *c*-axis deviates from the direction of the applied electric field, i.e., the x_3-axis

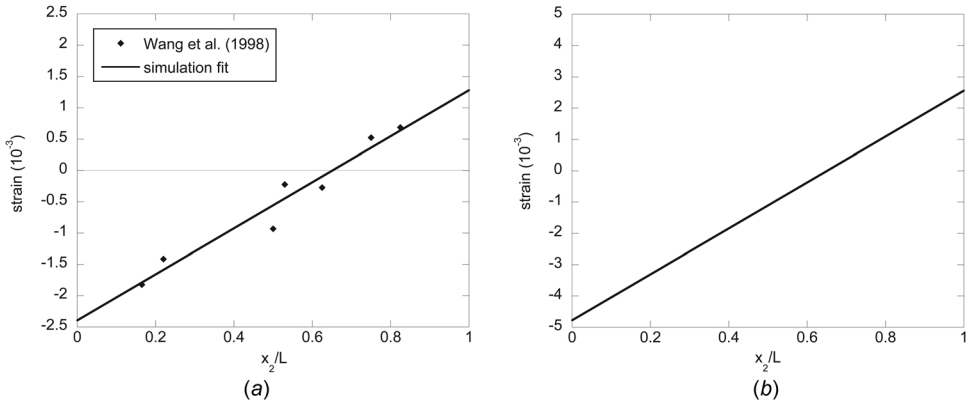

Fig. 5 (*a*) Linear fit to the data in Wang et al. [8] used to define the measured elastic strain $\varepsilon_{33}^{e(m)}$ to match using the algorithm in Sec. 3.2 and (*b*) resulting electromigration dilatational strain γ assuming grain boundary diffusion

this experiment, the strain ε_{33}^{e} was found to *decrease* (become more compressive) linearly along the direction of electron flow to a point and then became constant as shown in Fig. 2.

The following properties are used in the simulations. In both cases, the Al is columnar with a strong $\langle 111 \rangle$ fiber texture with the in-plane texture being fairly random. Thus, the Al may be treated as transversely isotropic with the axis of symmetry aligned in the x_3-direction. The elastic stiffness properties with respect to the sample coordinates for the Al computed from the single crystal properties are $C_{11} = C_{22} = 107.1$ GPa, $C_{33} = 108.7$ GPa, $C_{12} = 59.2$ GPa, $C_{13} = C_{23} = 57.5$ GPa, $C_{44} = C_{55} = 22.3$ GPa, and $C_{66} = (C_{11} - C_{12})/2 = 23.9$ GPa. There is a slight difference in the elastic properties at the two experimental temperatures, which is ignored here. The polycrystalline SiO_2 is treated as isotropic with elastic modulus and Poisson's ratio of $E_s = 75$ GPa and $\nu_s = 0.17$. In the Zhang et al. experiment, we also must consider the fine-grained layers with a mixture of Al and $TiAl_3$. The lower layer is estimated to be 90% $TiAl_3$, while the upper layer is estimated to be 20% $TiAl_3$, with the balance being fine Al grains. Treating each material as isotropic and taking volume average properties, the elastic modulus and Poisson's ratio for the material below the Al line are $E_b = 160$ GPa and $\nu_b = 0.26$ and for the material above the Al line are $E_a = 85$ GPa and $\nu_a = 0.33$. The resistivity is needed to back out $Z^{\star}$. For the Wang et al. [8] case, the resistivity for Al at 260 °C is $\rho = 5.50 \times 10^{-6}\ \Omega$ cm. For the Zhang et al. [9] case, the resistivity for Al at 190 °C is $\rho = 4.54 \times 10^{-6}\ \Omega$ cm. The atomic volume of Al is $\Omega = 1.66 \times 10^{-23}$ cm^3.

For both cases, we only model the material above the Si substrate, and we treat the Si substrate as rigid and the materials perfectly bonded to it. The outer surface of the SiO_2 is treated as traction free. Symmetry is assumed about the x_2–x_3 plane, and the domain is extended in the x_1-direction sufficiently such that the outer boundary, where a symmetry boundary condition is also applied, does not influence the solution.

First, we consider the wider line in Wang et al. [8]. We model the structure illustrated in Fig. 1(*a*) with 36,500 eight-node hexahedral elements. Since we do not know the exact grain structure, we treat the Al as homogeneous, but since we know it is multiple grains across the width and is very wide, we expect either grain boundary diffusion or surface diffusion along the top and bottom surfaces to dominate. We consider both these cases. For grain boundary diffusion, assuming equiaxed in plane grains, we assume $a_1 = a_2 = 0.5$ and $a_3 = 0$, and for surface diffusion, we assume $a_1 = a_2 = 0$ and $a_3 = 1$, in Eq. (4). For both cases, we match the linear fit to the elastic strain data shown in Fig. 5(*a*). After solving using the procedure described in Sec. 3.2, we find that when we assume surface diffusion, the electromigration dilatational strain γ is positive at the upstream end and negative at the downstream end. Intuitively, this is not reasonable because that would indicate that material is being deposited at the upstream end (cathode) and deplete at the downstream end (anode). On the other hand, assuming grain boundary diffusion, we obtain the inelastic dilatational strain shown in Fig. 5(*b*). As material is depleted in the x_1–x_2 plane at the upstream end, tensile stresses develop in this plane leading to a negative elastic strain in the x_3-direction, as observed in the experiments, due to the Poisson effect. The exact opposite occurs when the material is depleted in the x_3-direction, which does not match the experiments. From the resulting stress gradient along the length of the line, using Eq. (9), we compute $Z^{\star} = 2.5$ for grain boundary diffusion in Al lines.

Next, we consider the narrow line in Zhang et al. [9]. We model the structure illustrated in Fig. 1(*b*) with 5800 eight-node hexahedral elements. Again, we treat the Al grain structure as homogeneous. Since the line is only one grain across the width, we do not expect grain boundary diffusion to dominate, so we assume surface diffusion with $a_1 = a_2 = 0$ and $a_3 = 1$ initially. However, in this case we also have measurements of the deviatoric elastic strains. Thus, we also adjust the values for a_1, a_2, and a_3 to best fit the deviatoric elastic strains. While the entire deviatoric elastic strain tensor was measured along the length of the line, it was found that the shear components were relatively small, which confirms the assumption that the principal strain directions, both elastic and electromigration-induced inelastic, are along the global coordinate directions. Solving using the procedure in Sec. 3.2, we

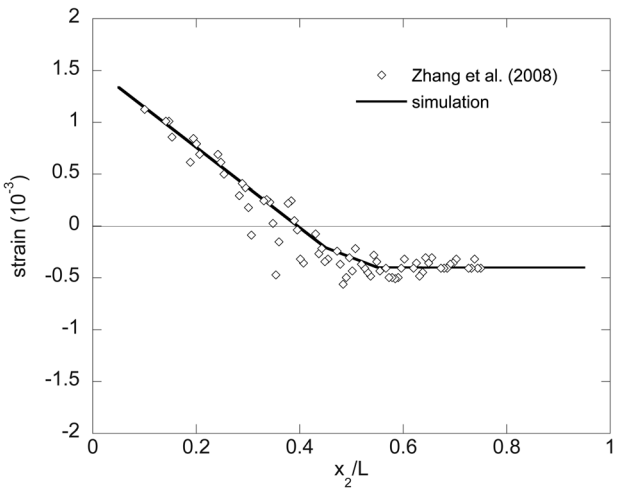

Fig. 6 Fit to the data in Zhang et al. [9] used to define the measured elastic strain $\varepsilon_{33}^{e(m)}$ to match using the algorithm in Sec. 3.2

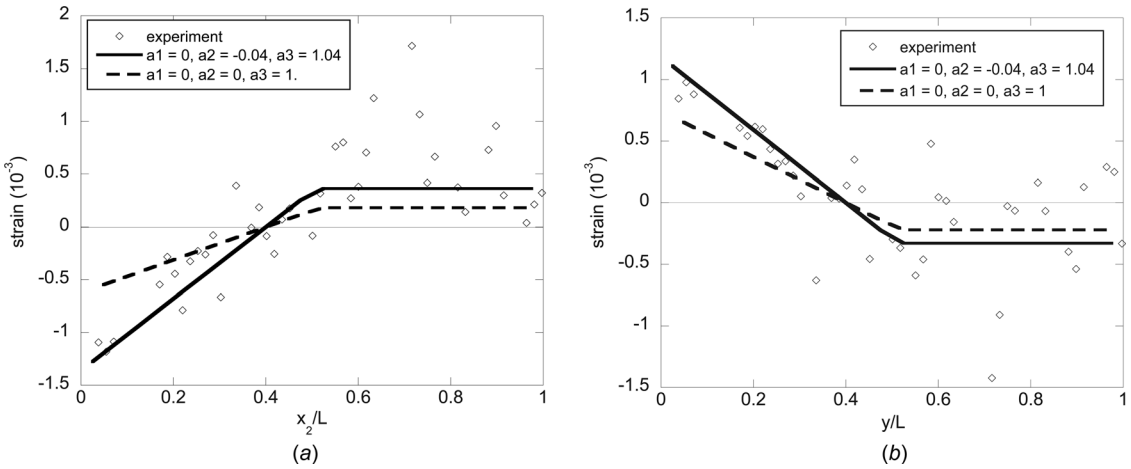

Fig. 7 Comparison of the measured and computed deviatoric elastic strain components for two different sets of values for a_1, a_2, and a_3 associated with different diffusion paths: (*a*) ε'^{e}_{22} and (*b*) ε'^{e}_{33}

find $a_1 = 0$, $a_2 = -0.04$, and $a_3 = 1.04$. The fit to the elastic strain data used is shown in Fig. 6, and the resulting fits to the deviatoric elastic strain components, ε'^{e}_{22} and ε'^{e}_{33}, are shown in Figs. 7(*a*) and 7(*b*). We can see that the small change in the a_i values greatly improved the fit to the deviatoric elastic strain data. At first, the fact that $a_2 < 0$ and $a_3 > 1$ may seem counterintuitive as it seems to indicate that material is accumulating along the x_2-direction while being depleted along the x_3-direction in the upstream end and vice versa in the downstream end. However, as material is depleted in the upstream end, a triaxial tensile stress state starts to develop, which creates tensile stresses on vertical grain boundaries that span the width of the line. For grain boundaries that are nearly perpendicular to the current direction, i.e., with normals along the x_2-direction, while there is no current-driven diffusion on these boundaries, the tensile stress on the grain boundaries will tend to pull diffusing atoms into the grain boundaries at the upstream end, and likewise, push diffusing atoms out of the grain boundaries at the downstream end where compressive stresses develop. From the resulting stress gradient along the line at the upstream end (ignoring the downstream end, where the line may have delaminated), using Eq. (9), we compute $Z^* = 1.2$ for surface diffusion between the Al and fine grain titanium rich layers.

5 Conclusions

A finite element based algorithm for computing the inelastic dilatational strain and displacement field resulting from electromigration and stress-driven diffusion that satisfied mechanical equilibrium was presented. In this work, plastic deformations were not considered, and the only inelastic deformation is that due to diffusion. The effect of anisotropic material behavior was considered.

The effect of the crystal orientation on the Blech limit was studied for Sn-based solder joints. In that work, the Blech limit was predicted to vary from $jL = 4.05$ A/cm to 14.11 A/cm, with the limit highest when the c-axis is aligned with the current direction and lowest when the c-axis is perpendicular to the current direction. These limits are within the range observed experimentally, but are low on average. This may be due to the fact the Blech limit was defined here as when 10% of the crystal yielded due to the resolved shear stress on a slip system exceeding the critical value. However, it is expected that the crystal can carry a higher load and may not fail until larger-scale yielding has occurred in the crystal. In future work, crystal plasticity will be considered to obtain a better estimate.

The effect of the grain structure on the effective diffusion paths and values for the effective charge number Z^* were predicted for passivated Al conductor lines by matching simulations to experimentally measured elastic strain components. It was found that for a wide line with multiple grains across the width, the dominant diffusion path is grain boundary diffusion and $Z^* = 2.5$, while for a narrow line with a single grain across the width (bamboo structure), the dominant diffusion path is surface diffusion and $Z^* = 1.2$ when the interface is with a fine-grained mixture of Al and $TiAl_3$.

Acknowledgment

This material was based upon the work supported by the National Science Foundation under Grant Nos. DMR-0312189 and DMR-1207291. The authors also thank Professor G. Slade Cargill, III, Fairchild Professor Emeritus from Lehigh University, for useful comments on the manuscript and for providing the experimental data on the aluminum lines.

References

[1] Fiks, V. B., 1959, "On Mechanism of Mobility of Ions in Metals," Sov. Phys. Solid State, **1**, pp. 14–28.
[2] Huntington, H. B., and Grone, A. R., 1961, "Current-Induced Marker Motion in Gold Wires," J. Phys. Chem. Solids, **20**, pp. 76–87.
[3] Black, J. R., 1969, "Electromigration—A Brief Survey and Some Recent Results," IEEE Trans. Electron. Dev., **16**(4), pp. 338–347.
[4] Blech, I. A., and Tai, K. L., 1977, "Measurement of Stress Gradients Generated by Electromigration," Appl. Phys. Lett., **30**(8), pp. 387–389.
[5] Blech, I. A., 1976, "Electromigration in Thin Aluminum Films on Titanium Nitride," J. Appl. Phys., **47**(4), pp. 1203–1208.
[6] Blech, I. A., and Herring, C., 1976, "Stress Generation by Electromigration," Appl. Phys. Lett., **29**(3), pp. 131–133.
[7] Hau-Riege, S. P., and Thompson, C. V., 2000, "The Effect of the Mechanical Properties of the Confinement Material on EM in Metallic Interconnects," J. Mater. Res., **15**(8), pp. 1797–1802.
[8] Wang, P.-C., Cargill, G. S., III, Noyan, I. C., and Hu, C.-K., 1998, "Electromigration-Induced Stress in Aluminum Conductor Lines Measured by X-Ray Microdiffraction," Appl. Phys. Lett., **72**(11), pp. 1296–1298.
[9] Zhang, H., Cargill, G. S., III, Ge, Y., Maniatty, A. M., and Liu, W., 2008, "Strain Evolution in Al Conductor Lines During Electromigration," J. Appl. Phys., **104**(12), p. 123533.
[10] Tu, K. N., 1994, "Irreversible Processes of Spontaneous Whisker Growth in Bimetallic Cu–Sn Thin-Film Reactions," Phys. Rev. B Condens. Matter, **49**(3), pp. 2030–2034.
[11] Li, S., and Basaran, C., 2009, "Effective Diffusivity of Lead Free Solder Alloys," Comput. Mater. Sci., **47**(1), pp. 71–78.
[12] Wang, Y., Lu, K. H., Gupta, V., Stiborek, L., Shirley, D., Chae, S.-H., Im, J., and Ho, P. S., 2012, "Effects of Sn Grain Structure on the Electromigration of Sn–Ag Solder Joints," J. Mater. Res., **27**(08), pp. 1131–1141.
[13] Tasooji, A., Lara, L., and Lee, K., 2014, "Effect of Grain Boundary Misorientation on Electromigration in Lead-Free Solder Joints," J. Electron. Mater., **43**(12), pp. 4386–4394.
[14] Lee, K., Kim, K.-S., Tsukada, Y., Suganuma, K., Yamanaka, K., Kuritani, S., and Ueshima, M., 2011, "Influence of Crystallographic Orientation of Sn–Ag–Cu on Electromigration in Flip-Chip Joint," Microelectron. Reliab., **51**(12), pp. 2290–2297.
[15] Dyson, B. F., Anthony, T. R., and Turnbull, D., 1967, "Interstitial Diffusion of Copper in Tin," J. Appl. Phys., **38**(8), p. 3408.

[16] Wu, A. T., and Hsieh, Y. C., 2008, "Electromigration-Induced Grain Rotation in Anisotropic Conducting Beta Tin," Appl. Phys. Lett., **92**(12), p. 121921.
[17] Lu, M., Shih, D.-Y., Lauro, P., Goldsmith, C., and Henderson, D. W., 2008, "Effect of Sn Grain Orientation on Electromigration Degradation Mechanism in High Sn-Based Pb-Free Solders," Appl. Phys. Lett., **92**(21), p. 211909.
[18] Korhonen, M. A., Borgesen, P., Tu, K. N., and Li, C. Y., 1993, "Stress Evolution Due to Electromigration in Confined Metal Lines," J. Appl. Phys., **73**(8), pp. 3790–3799.
[19] Ye, H., Basaran, C., and Hopkins, D., 2004, "Deformation of Solder Joint Under Current Stressing and Numerical Simulation—I," Int. J. Solids Struct., **41**(18–19), pp. 4939–4958.
[20] Ye, H., Basaran, C., and Hopkins, D., 2004, "Deformation of Solder Joint Under Current Stressing and Numerical Simulation—II," Int. J. Solids Struct., **41**(18–19), pp. 4959–4973.
[21] Li, S., Abdulhamid, M. F., and Basaran, C., 2009, "Damage Mechanics of Low Temperature Electromigration and Thermomigration," IEEE Trans. Adv. Packag., **32**, pp. 478–485.
[22] Singh, N., Bower, A. F., and Shankar, S., 2010, "A Three-Dimensional Model of Electromigration and Stress Induced Void Nucleation in Interconnect Structures," Modell. Simul. Mater. Sci. Eng., **18**(6), p. 065006.
[23] Liu, S., and Liu, Y., 2011, *Modeling and Simulation for Packaging Assembly: Manufacturing, Reliability and Testing*, Wiley, Singapore.
[24] Hao, J., Liu, Y., Rioux, M., and Zhang, A. L. L., 2011, "Electromigration Prediction and Test for 0.18 μm Power Technology in Wafer Level Reliability," IEEE Electronic Components and Technology Conference (ECTC), Lake Buena Vista, FL, May 31–June 3, pp. 1934–1938.
[25] Liu, Y., Zhang, Y., and Liang, L., 2010, "Prediction of Electromigration Induced Voids and Time to Failure or Solder Joint of a Wafer Level Chip Scale Package," IEEE Trans. Comput. Packag. Technol., **33**, pp. 544–552.
[26] Dandu, P., Fan, X. J., Liu, Y., and Diao, C., 2010, "Finite Element Modelling on Electromigration of Solder Joints in Wafer Level Packaging," Microelectron. Reliab., **50**(4), pp. 547–555.
[27] Liu, Y., Luk, T., and Irving, S., 2009, "Parameter Modeling for Wafer Probe Test," IEEE Electron. Packag. Manuf., **32**, pp. 81–88.
[28] Liu, Y., Liang, L., Irving, S., and Luk, T., 2008, "3D Modeling of Electromigration Combined With Thermal–Mechanical Effect for IC Device and Package," Microelectron. Reliab., **48**(6), pp. 811–824.
[29] Gleixner, R. J., and Nix, W. D., 1999, "A Physically Based Model of Electromigration and Stress-Induced Void Formation in Microelectronic Interconnects," J. Appl. Phys., **86**(4), pp. 1932–1944.
[30] Povirk, G. L., 1997, "Numerical Simulations of Electromigration and Stress-Driven Diffusion in Polycrystalline Interconnects," Mater. Res. Soc. Symp. Proc., **473**, pp. 337–342.
[31] Bower, A., and Freund, L., 1993, "Analysis of Stress-Induced Void Growth Mechanisms in Passivated Interconnect Lines," J. Appl. Phys., **74**(6), pp. 3855–3868.
[32] Bower, A., and Craft, D., 1998, "Analysis of Failure Mechanisms in the Interconnect Lines of Microelectronic Circuits," Fatigue Fract. Eng. Mater. Struct., **21**, pp. 611–630.
[33] Buchovecky, E., Jadhav, N., Bower, A. F., and Chason, E., 2009, "Finite Element Modeling of Stress Evolution in Sn Films Due to Growth of the Cu_6Sn_5 Intermetallic Compound," J. Electron. Mater., **38**(12), pp. 2676–2684.
[34] Wilkening, J., Borucki, L., and Sethian, J. A., 2004, "Analysis of Stress-Driven Grain Boundary Diffusion. Part II: Degeneracy," SIAM J. Appl. Math., **64**, pp. 1864–1886.
[35] Sarychev, M. E., Zhitnikov, Y. V., Borucki, L., Liu, C.-L., and Makhviladze, T., 2000, "A New, General Model for Mechanical Stress Evolution During Electromigration," Thin Solid Films, **365**(2), pp. 211–218.
[36] Maniatty, A., Liu, Y., Klaas, O., and Shephard, M., 2002, "Higher Order Stabilized Finite Element Method for Hyperelastic Finite Deformation," Comput. Methods Appl. Mech. Eng., **191**, pp. 1491–1503.
[37] Lu, M., Shih, D.-Y., Lauro, P., and Goldsmith, C., 2009, "Blech Effect in Pb-Free Flip Chip Solder Joint," Appl. Phys. Lett., **94**(1), p. 011912.
[38] Huntington, H. B., 1975, "Effect of Driving Forces on Atom Motion," Thin Solid Films, **25**(2), pp. 265–280.
[39] Puttlitz, K. J., and Stalter, K. A., 2004, *Handbook of Lead-Free Solder Technology for Microelectronic Assemblies*, Marcel Dekker, New York.
[40] Rayne, J. A., and Chandrasekhar, B. S., 1960, "Elastic Constants of β Tin From 4.2 K to 300 K," Phys. Rev., **120**(5), pp. 1658–1663.
[41] Zhou, B., Bieler, T. R., Lee, T.-K., and Liu, K.-C., 2009, "Methodology for Analyzing Slip Behavior in Ball Grid Array Lead-Free Solder Joints After Simple Shear," J. Electron. Mater., **38**(12), pp. 2702–2711.
[42] Vellinga, W. P., Martin, M. A., and Geers, M. G. D., 2006, "Microstructure Evolution in a Pb-Free Solder Alloy During Mechanical Fatigue," Mater. Sci. Eng. A, **431**(1–2), pp. 166–174.